

1 **Cross Section Measurement of ${}^9\text{Be}(\gamma, n){}^8\text{Be}$ and Implications for**
 2 **$\alpha + \alpha + n \rightarrow {}^9\text{Be}$ in the r-Process**

3 C.W. Arnold,^{*} T.B. Clegg, C. Iliadis, H.J. Karwowski, G.C. Rich, and J.R. Tompkins

4 *Department of Physics and Astronomy,*

5 *University of North Carolina at Chapel Hill, Chapel Hill, NC 27599 and*

6 *Triangle Universities Nuclear Laboratory (TUNL), Durham, NC 27708[†]*

7 C.R. Howell

8 *Department of Physics, Duke University, Durham, NC 27708 and*

9 *Triangle Universities Nuclear Laboratory (TUNL), Durham, NC 27708[†]*

10 (Dated: November 12, 2018)

11 **Abstract**

12 Models of the r-process are sensitive to the production rate of ${}^9\text{Be}$ because, in explosive en-
 13 vironments rich in neutrons, $\alpha(\alpha n, \gamma){}^9\text{Be}$ is the primary mechanism for bridging the stability
 14 gaps at $A = 5$ and $A = 8$. The $\alpha(\alpha n, \gamma){}^9\text{Be}$ reaction represents a two-step process, consisting
 15 of $\alpha + \alpha \rightarrow {}^8\text{Be}$ followed by ${}^8\text{Be}(n, \gamma){}^9\text{Be}$. We report here on a new absolute cross section
 16 measurement for the ${}^9\text{Be}(\gamma, n){}^8\text{Be}$ reaction conducted using a highly-efficient, ${}^3\text{He}$ -based neutron
 17 detector and nearly-monoenergetic photon beams, covering energies from $E_\gamma = 1.5$ MeV to 5.2
 18 MeV, produced by the High Intensity γ -ray Source of Triangle Universities Nuclear Laboratory.
 19 In the astrophysically important threshold energy region, the present cross sections are 40% larger
 20 than those found in most previous measurements and are accurate to $\pm 10\%$ (95% confidence).
 21 The revised thermonuclear $\alpha(\alpha n, \gamma){}^9\text{Be}$ reaction rate could have implications for the r-process in
 22 explosive environments such as Type II supernovae.

23 PACS numbers: 26.30.Hj, 25.20.-x, 27.20.+n

^{*} arnold@lanl.gov; Present address: Los Alamos National Laboratory, P.O. Box 1663, Los Alamos, NM
 87545

[†] <http://www.tunl.duke.edu>

24 I. INTRODUCTION

25 The r-process likely happens in supernovae [1], in neutron star mergers [2], or some other
26 high temperature ($T \geq 1$ GK) and high neutron flux ($\phi \geq 10^{20}$ cm⁻²s⁻¹) environment. At
27 present, the case for an indisputable r-process site has not been made, and recent arguments
28 point out the necessity of multiple sites [3]. Supernovae have long been cited as potential
29 r-process factories because they produce the necessary explosive conditions and they occur
30 frequently enough to produce substantial abundances. The production of heavy nuclides
31 arising from explosive nucleosynthesis at a Type II supernova site is linked to the rate of
32 ⁹Be production [4].

33 The behavior of a core-collapse supernova has been described, for example, by Woosley
34 and Janka [5]. A star of 8 to 25 M_{\odot} passes through the stages of hydrogen, helium, carbon,
35 neon, oxygen, and silicon burning at its core, continuously growing hotter and more dense.
36 It eventually forms an iron-group core of Chandrasekhar mass ($\approx 1.4 M_{\odot}$). Since the core
37 has no other source of thermonuclear energy to support the pressure, it collapses. Energy
38 is released in the form of neutrino radiation, while the collapse is accelerated by electron
39 captures and photodisintegrations. An Earth-sized iron-core collapses with a velocity of
40 $\sim c/4$ into a single, neutron-rich nucleus about 30 km in diameter. The collapse generates
41 a rebounding shock wave, which ultimately stalls as it attempts to push through the in-
42 falling matter. The proto-neutron star briefly continues accreting matter, while radiating
43 $\sim 10^{46}$ J in the form of neutrinos, accounting for nearly 10% of its rest mass. At this stage,
44 convection, rotation, and magnetism likely contribute to the dynamics of the subsequent
45 explosion. However, self-consistent, three-dimensional models that predict explosion remain
46 elusive [6].

47 A. The r-process

48 The r-process produces about half of the nuclides heavier than iron [5]. It requires a hot,
49 neutron-dense environment where neutron captures occur so rapidly that the nucleosynthesis
50 path is pushed far out to the neutron-rich side beyond the stability valley. After cessation
51 of the neutron flux, the short-lived nuclei β -decay to stable species.

52 Preceding the r-process is the α -process [7], which is driven by charged-particle reactions

53 and takes place when the shock has cooled from 5 GK to 3 GK over a time period of a few
54 seconds. In this stage of nucleosynthesis a reaction path is needed to bridge the stability
55 gaps at $A = 5$ and $A = 8$; the most efficient path is $\alpha + \alpha \rightarrow {}^8\text{Be}$ and ${}^8\text{Be}(n, \gamma){}^9\text{Be}$, followed
56 by ${}^9\text{Be} + \alpha \rightarrow {}^{12}\text{C} + n$ [8]. As cooling continues this reaction sequence largely establishes the
57 neutron-to-seed-nucleus ratio to which the subsequent r-process is very sensitive [9]. Too
58 few seed nuclei will under-produce r-process nuclei, while too many seed nuclei produced in
59 the α -process will starve the r-process environment of neutrons. Since r-process abundance
60 predictions in certain stellar models are extremely sensitive to the $\alpha(\alpha n, \gamma){}^9\text{Be}$ rate [4, 10,
61 11], establishing a precise rate for the formation of ${}^9\text{Be}$ via the $\alpha(\alpha n, \gamma){}^9\text{Be}$ reaction is
62 required for accurately modeling nucleosynthesis in supernovae.

63 The ${}^9\text{Be}(\gamma, n){}^8\text{Be}$ reaction may be used to deduce the ${}^8\text{Be}(n, \gamma){}^9\text{Be}$ cross-section by
64 applying the reciprocity theorem. Previous ${}^9\text{Be}$ photodisintegration studies are numerous
65 [12–26] but reveal relatively large cross-section uncertainties in the astrophysically important
66 region near the neutron emission threshold. New (γ, n) cross-section measurements with
67 improved accuracy are now possible using intense photon beams with small energy spreads
68 and neutron detectors with large solid angle coverage and high efficiencies.

69 In the following, Sect. II describes a new measurement of ${}^9\text{Be}(\gamma, n){}^8\text{Be}$ and provides de-
70 tails of the data analysis used to obtain cross sections. Section III describes the methods used
71 to extract resonance parameters from the new data using proper energy dependences for par-
72 tial widths of ${}^9\text{Be}$ excited states. The methods employed to calculate the ${}^8\text{Be}(n, \gamma){}^9\text{Be}$ cross
73 section and the corresponding $\alpha(\alpha n, \gamma){}^9\text{Be}$ reaction rates are described in Sect. IV, along
74 with a comparison of the determined rates with those from earlier studies. Finally, Sect. V
75 presents a summary of the findings presented in this paper.

76 II. EXPERIMENT

77 Collimated, near-monoenergetic photon beams of $1.5 \text{ MeV} \leq E_\gamma \leq 5.2 \text{ MeV}$ were incident
78 on a thick ${}^9\text{Be}$ target located within the central bore of the neutron detector. The abso-
79 lute number of neutrons from the (γ, n) reaction was determined using a moderated ${}^3\text{He}$
80 proportional counter with a high efficiency ($\sim 60\%$) for detecting low-energy neutrons [27].
81 The absolute incident photon flux was measured using a large NaI(Tl) detector. Photon
82 beam energy resolution was determined with a high purity germanium (HPGe) detector. A

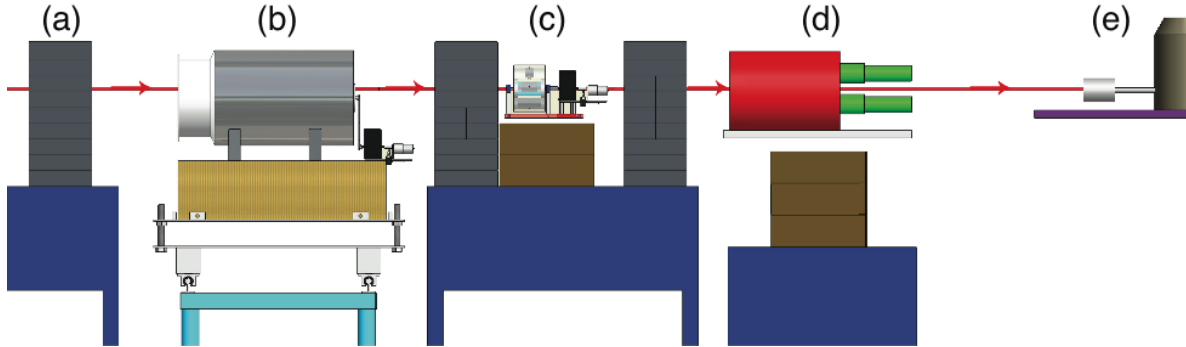


FIG. 1. Schematic diagram of the experimental setup for the ${}^9\text{Be}(\gamma, n){}^8\text{Be}$ reaction measurements. After collimation, the photon beam passes through scintillation paddles (not shown) and into the target room. The photon beam then passes through the following elements: (a) “clean-up” collimator wall; (b) the chosen target located near the longitudinal center of the neutron counter; (c) lead attenuators located between lead collimator walls; (d) NaI(Tl) detector; (e) HPGe detector.

83 schematic diagram of the experimental setup is shown in Fig. 1.

84 A. Experimental setup

85 Intense, collimated photon beams ($\phi \approx 3 \times 10^7 \gamma/\text{s}$) are routinely produced at the Tri-
 86 angle Universities Nuclear Laboratory’s High Intensity Gamma Source (HI γ S) by inverse-
 87 Compton scattering of free-electron-laser photons from electron bunches circulating in a
 88 storage ring [28]. For the present experiment, a circularly-polarized beam was used and some
 89 flux was sacrificed to attain the high photon energy resolution needed to map the detailed
 90 behavior of the cross section at the three-body (1573 keV) and two-body (1665 keV) thresh-
 91 olds shown in Fig. 2. Present data were taken using beam intensities of $10^5 \leq \phi \leq 10^6 \gamma/\text{s}$ and
 92 energy spreads of $\leq 1\%$.

93 The photon beam was defined by a 12-mm diameter, 30.5-cm thick lead collimator. It
 94 then passed successively through three thin scintillating paddles that acted as a relative
 95 photon flux monitor, a 2.54-cm diameter hole in a lead “clean-up” collimator (CC), and
 96 ~ 1.5 m of air before reaching a second CC (shown as (a) in Fig. 1) placed directly in front
 97 of the neutron detector.

98 At each energy, photons impinged successively on one of three thick, 19-mm diameter
 99 cylindrical targets (${}^9\text{Be}$, D_2O , graphite) described in Table I, or air, as they passed through

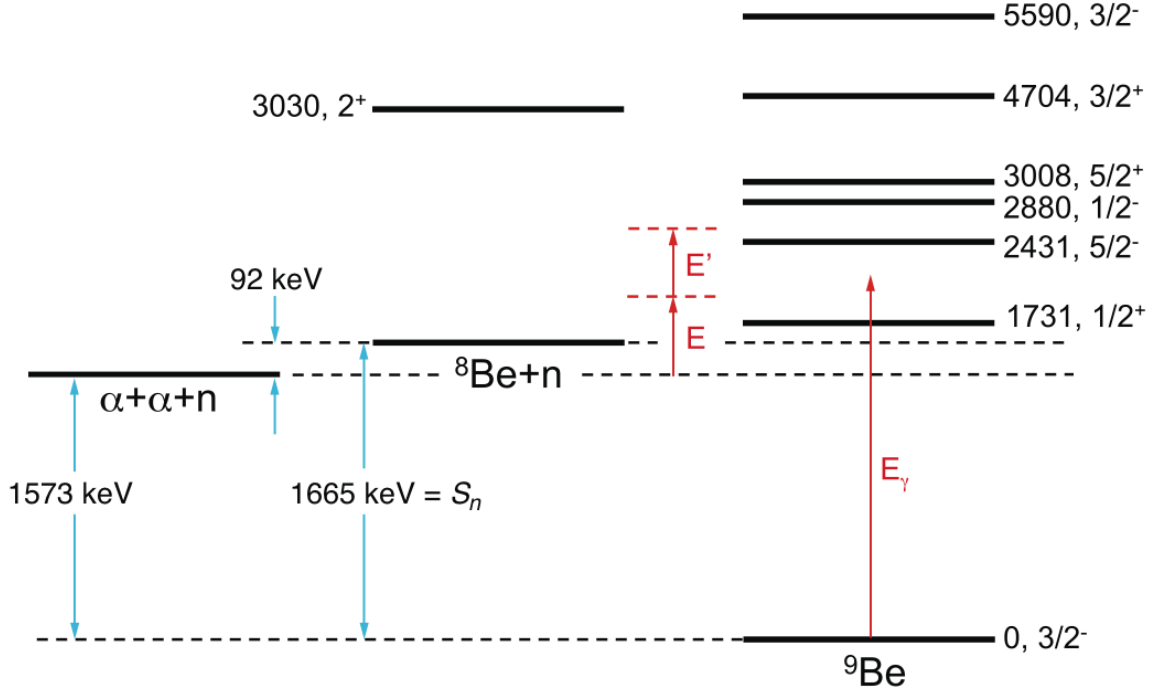


FIG. 2. (Color Online) A level scheme relating the mass energies of $\alpha + \alpha + n$, ${}^8\text{Be} + n$, and ${}^9\text{Be}$. Thresholds for three-body and two-body breakup of ${}^9\text{Be}$ are shown to occur at incident γ -ray energies E_γ of 1573 keV and 1665 keV, respectively. The latter is also the neutron separation energy S_n for ${}^9\text{Be}$. Energies shown for ${}^9\text{Be}$ excited states are from the present work. In the rate calculation (described in Sect. IV), E is the center-of-mass energy of the two α -particles. The parameter E' is the energy of the ${}^8\text{Be}$ nucleus and the neutron with respect to E . In this scheme, formation of ${}^9\text{Be}$ at $E = E' = 0$ is very unlikely, but not prohibited because the ground state of ${}^8\text{Be}$ has finite width.

TABLE I. Targets used in the present experiment and their physical properties.

Material	Length (cm)	Density (g cm ⁻³)	Mass (g mol ⁻¹)	Thickness (nuclei cm ⁻²)
${}^9\text{Be}$	2.54	1.848	9.012	3.14×10^{23}
Graphite	2.54	1.700	12.01	2.89×10^{23}
D ₂ O	7.59	1.106	20.04	5.05×10^{23}

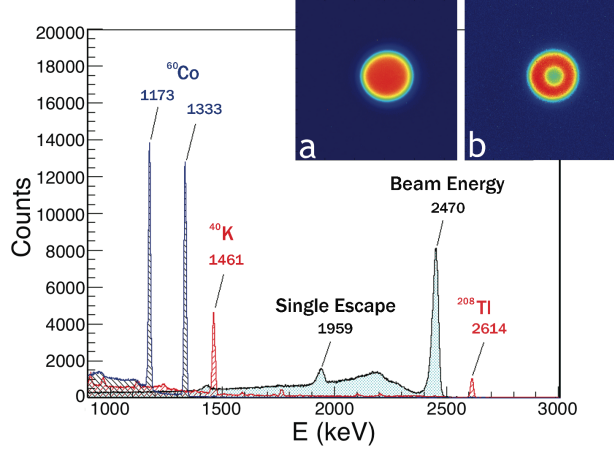


FIG. 3. (Color Online) A HPGe spectrum for 2470-keV photon beam with a resolution of $\Delta E/E = 1\%$. Spectra obtained with ^{60}Co , ^{40}K , and ^{208}Tl calibration sources are overlaid. Images showing confirmation of target alignment are inset. (a) An unattenuated beam profile. Flux was nearly constant across the 12-mm diameter and decreased rapidly at the edges. (b) Contrast from a 4-mm diameter lead alignment pellet confirmed the axial placement of the target.

100 the neutron detector. The heavy water target was bombarded under the same experimental
 101 conditions as the ^9Be target, allowing for normalization of the $^9\text{Be}(\gamma, n)^8\text{Be}$ measurements
 102 to the well-known $^2\text{H}(\gamma, n)^1\text{H}$ cross section [29] and for calibration of the neutron detector
 103 efficiency. The graphite target was used to determine beam-induced backgrounds in the
 104 neutron detector.

105 To increase the efficiency of data collection, targets were remotely rotated into the beam
 106 using a four-position Geneva mechanism, which also assured reproducible alignment of the
 107 axis of each cylindrical target sample with the beam axis. Axial alignment of the target was
 108 confirmed using an alignment pellet and a photon beam imaging system [30] (see Fig. 3).

109 Downstream of the target, lead of various thicknesses could be inserted to attenuate the
 110 beam by up to a factor of 100. Further downstream, the remaining photons were incident on
 111 either a NaI(Tl) detector or a HPGe detector, depending on whether photon flux or energy
 112 was being measured. The lead attenuators facilitated simultaneous high neutron counting
 113 rates and negligible NaI(Tl) signal pile-up. Data acquisition dead-times were assured to be
 114 small. The counts measured in the NaI(Tl) detector were corrected for detection efficiency
 115 as well as for attenuation through the lead and targets.

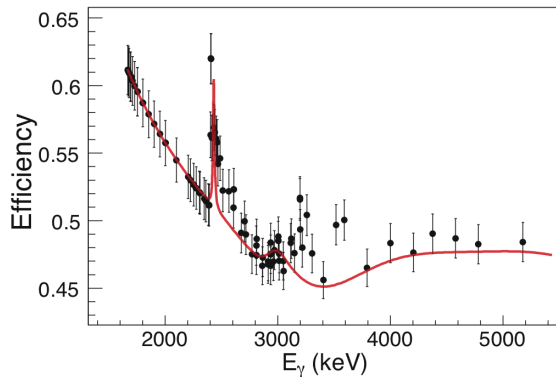


FIG. 4. (Color Online) Effective neutron detector efficiency versus photon energy for ${}^9\text{Be}(\gamma, n){}^8\text{Be}$ with error bars representing the 4.6% systematic uncertainty. Above $E_\gamma = 2431$ keV, average neutron energy, and thus detection efficiency, was determined using the experimental I/O ratio. The (red) curve is modeled using Eq. 1 with the branching ratios listed in Table II. Discrepancies in the 3 to 4 MeV range are not well understood, but do not affect the present calculation for the astrophysical $\alpha(\alpha n, \gamma){}^9\text{Be}$ reaction rate discussed in Sect. IV.

116 B. Detector calibration

117 Absolute measurements of the number of photons on target and the number of emitted
 118 neutrons from the reaction were needed to determine the total cross section of ${}^9\text{Be}(\gamma, n){}^8\text{Be}$.
 119 Thus, it was essential to determine the absolute energy-dependent detection efficiencies of
 120 the neutron detector and the large NaI(Tl) detector. The active neutron detection elements
 121 were 18 tubular proportional counters, each containing ${}^3\text{He}$ at 6.1×10^5 Pa. The tubes,
 122 embedded in a cylindrical polyethylene body that served as a neutron moderator, were
 123 arranged in concentric inner (I) and outer (O) rings of nine equally spaced detectors each.
 124 The energy-dependent efficiency of the neutron counter was determined in an extensive
 125 study [27]. The ratio of counts in the inner and outer rings (I/O ratio) provided a coarse
 126 estimate of the average neutron energy.

127 The total efficiency of the large NaI(Tl) detector was found to be nearly constant ($98.3 \pm$
 128 1.7%) over the experimental energy range using the Monte-Carlo codes GEANT4 and MCNPX.
 129 The results were consistent with data obtained using the ${}^{19}\text{F}(p, \alpha\gamma)$ reaction, taken using a
 130 mini-tandem accelerator [31]. This measurement provided a determination of the absolute
 132 detection efficiency for 6.13 MeV photons [32, 33].

133 While the efficiency of the large NaI(Tl) detector was constant for photons within the
 134 experimental energy range, the effective efficiency of the neutron detector for photoneutrons
 135 from ${}^9\text{Be}$, $\epsilon_{\text{eff}}(E_\gamma)$, varied and is shown in Fig. 4. As can be seen in Fig. 2, the average
 136 energy for neutrons which decay to the ground state of ${}^8\text{Be}$ is $E_\gamma - S_n$, and for these neutrons
 137 the detection efficiency ϵ_n may be described using a sixth-order polynomial in E_n . Above
 138 $E_\gamma = 2431$ keV, multiple decay channels exist and the average neutron energy is no longer
 139 proportional to the photon energy. Instead, it becomes nonlinear and strongly dependent
 140 on the photon energy, which causes ϵ_{eff} to deviate from the polynomial that describes ϵ_n . To
 141 account for this, the effective efficiency was described using

$$\begin{aligned} \epsilon_{\text{eff}}(E_\gamma) = & \epsilon_n(E_\gamma - S_n) \left(\sum_j \frac{\beta_j \sigma_j}{\sigma_{\text{tot}}} \right) + \\ & \epsilon_n(\delta E_n) \left(\sum_j \frac{(1 - \beta_j) \sigma_j}{\sigma_{\text{tot}}} \right), \end{aligned} \quad (1)$$

142 where for level j , σ_j is the contribution from state j to the total cross section σ_{tot} , and β_j is a
 143 branching ratio for state j to the ground state of ${}^8\text{Be}$. This form assumes that a newly opened
 144 neutron branch will decay with a small neutron energy δE_n . The detection efficiency for the
 145 fraction of the total cross-section decaying to the ground state is described by the simple
 146 polynomial $\epsilon_n(E_\gamma - S_n)$, while the efficiency of new branches is $\epsilon_n(\delta E_n) \approx \epsilon_{\text{max}}$. This model
 147 is compared in Fig. 4 to a point-by-point determination of the neutron detector efficiency
 148 constructed using the I/O ratio. The branching ratio for the $5/2^-$ state at 2431 keV was
 149 taken from Ref. [34]. Other branching ratios were chosen to make the model congruent
 150 with the point-by-point analysis. The contribution of states other than the $1/2^+$ state to
 151 the $\alpha(\alpha n, \gamma){}^9\text{Be}$ rate will be shown in Sect. IV to be nearly independent of the choice of
 152 branching ratios.

153 C. Data analysis

154 We performed two analyses of the yield data: (i) assuming a monoenergetic photon beam;
 155 and (ii) assuming a photon beam with a finite energy width, requiring deconvolution of the
 156 photon beam energy profile to interpret the neutron yield accurately.

157 Under the assumption of a monoenergetic beam, the cross section may be written as

$$\sigma = \frac{N_n}{N_\gamma \cdot (N_T/A) \cdot \epsilon_n}, \quad (2)$$

158 where N_n is the number of detected neutrons, N_γ is the number of incident photons, N_T/A is
 159 the effective number of target nuclei per unit area, and ϵ_n is the neutron detector efficiency.
 160 The quantity N_T/A was determined by comparing neutron yields from target-in and target-
 161 out runs. Thick targets required a photon energy-dependent correction of the form

$$\eta = \frac{1 - e^{-\mu t}}{\mu t}, \quad (3)$$

162 where μ is a material specific attenuation coefficient and t is the thickness of the target.
 163 This correction accounted for the reduction in the number of incident photons caused by
 164 interactions within the target volume.

165 Total ${}^9\text{Be}(\gamma, n){}^8\text{Be}$ cross-section uncertainties for σ in Eq. 2 were found to be 3.2%
 166 (statistical) and 4.6% (systematic). The largest contributions to the uncertainties came
 167 from the absolute efficiencies of the neutron and NaI(Tl) detectors and the exact photon
 168 beam flux loss associated with lead attenuators. Numerical values for cross sections and a
 169 detailed analysis of the associated experimental uncertainties are available in Ref. [32].

170 The second analytic approach treated the reality that the photon beam was not truly
 171 monoenergetic. Such a treatment is especially important near threshold, where the cross
 172 section changed significantly within the energy spread of the beam (see Fig. 5). The
 173 experimental yield Y may be defined as

$$Y = \frac{\int f \cdot \sigma_t \cdot \epsilon_n \cdot (N_T/A) dE_\gamma}{\int f dE_\gamma} = \frac{N_n}{N_\gamma}, \quad (4)$$

174 where f is an energy-dependent function describing the energy distribution of the pho-
 175 ton beam and σ_t is a trial cross section.

176 To determine f , the detector response function was deconvolved from the HPGe spectrum
 177 at each beam energy. The resulting spectra were then normalized such that

$$\int f dE_\gamma = N_\gamma, \quad (5)$$

178 where N_γ was determined using the NaI(Tl) detector. The trial cross section σ_t was assumed
 179 to be the sum of six Breit-Wigner equations (BWEs), each of which had three free parameters
 180 corresponding to the resonance energy E_R , the neutron partial width Γ_n , and the transition
 181 strength B(E1) or B(M1) of an excited state in ${}^9\text{Be}$.

182 Histograms were constructed for the other components of $Y(\sigma, \epsilon_n, N_t/A)$ as a function of
 183 photon energy. Each bin of the histogram then represented the respective component of the

184 yield over dE , the width of the bin. Thus, the calculated yield Y^* was given by

$$Y^* = \frac{\sum_i f_i \cdot \sigma_i \cdot \epsilon_{ni}(N_t/A)_i}{\sum_i f_i}, \quad (6)$$

185 where the width of the i^{th} bin was ~ 1.6 keV. In this way the yield-weighted *effective* energy,
186 E_γ^* was defined as,

$$E_\gamma^* = \frac{\sum_i E_{\gamma_i} f_i \cdot \sigma_i \cdot \epsilon_{ni}(N_t/A)_i}{\sum_i f_i \cdot \sigma_i \cdot \epsilon_{ni}(N_t/A)_i}. \quad (7)$$

187 The trial cross section was then iteratively adjusted (over ~ 8 steps) until the global devia-
188 tion between the calculated yield and the experimental yield was minimized. This process
189 resulted in a deconvoluted cross section shown in Fig. 5 along with that deduced from
190 the monoenergetic beam analysis. Figure 6 shows a histogram of the deviations between
191 experimental yields and yields calculated from the deconvoluted cross section for 52 data
192 points. The relative error is within $\pm 5\%$ at the 68% confidence interval and $\pm 10\%$ at the
193 95% confidence interval.

196 D. The ${}^9\text{Be}(\gamma, n){}^8\text{Be}$ cross section

197 From the two-body threshold energy of $E_{Th} = S_n = 1665$ keV to 1900 keV, the present
198 cross sections are larger than most of the previously reported data. Notice in Fig. 5 that
199 deconvolution changes the shape of the cross section at the threshold, transferring strength
200 from below to above E_{Th} . The need for deconvolution could well explain some disagreement
201 in this region with yields measured in earlier experiments using photon beams having larger
202 energy spreads than those used in the present experiment [22, 25].

203 The narrow $5/2^-$ state at 2431 keV was far better resolved in the present experiment
204 than in previous works. The present experimental yield peaks more than a factor of 3 above
205 the peak measured by Ref. [25] and nearly a factor of 2 above that of Ref. [22]. The present
206 data, over the broad $1/2^-$ and $5/2^+$ resonances near 3 MeV, are in fair agreement with the
207 data of Refs. [18, 22] but not in agreement with the results of Ref. [25] which were obtained
208 with a large photon beam energy spread.

209 At energies above the broad peak at 3 MeV the present data agree with Refs. [18, 25],
210 but not with Ref. [22]. A $3/2^+$ state at 4.7 MeV and a $3/2^-$ state at 5.6 MeV are the next

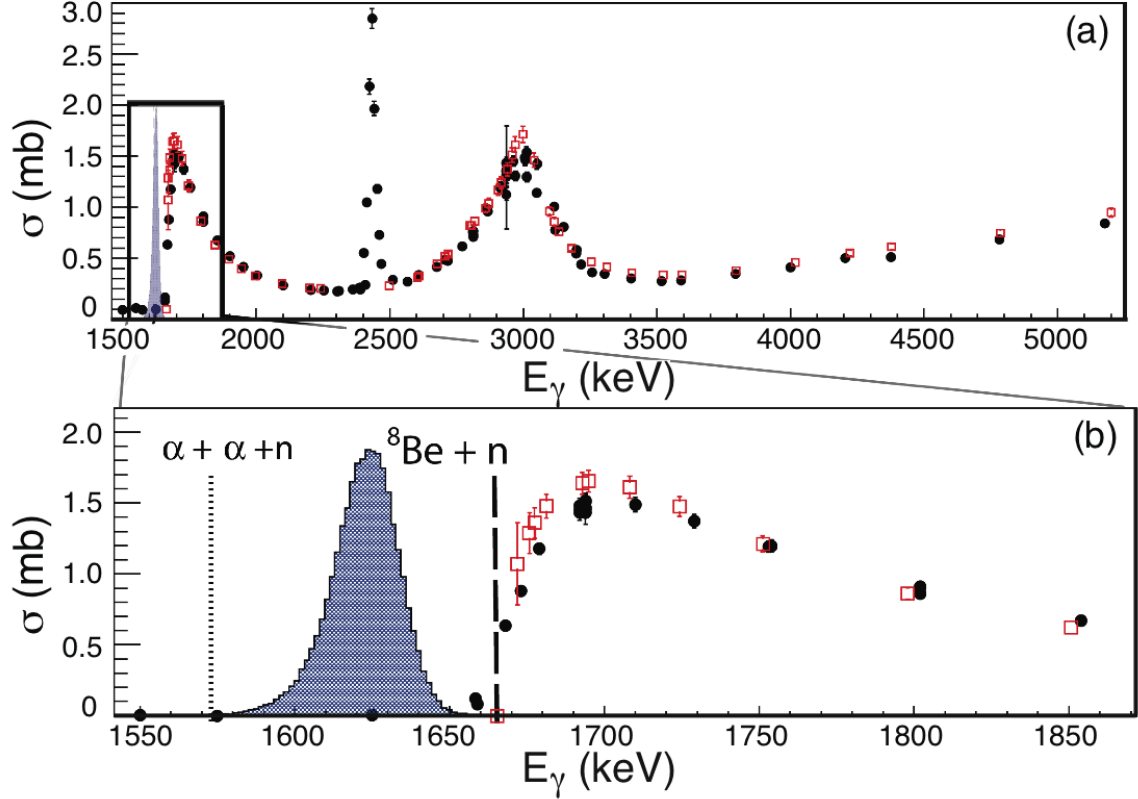


FIG. 5. (Color Online) A plot of monoenergetic beam cross sections (black dots) and deconvoluted cross sections (open red squares). Error bars are shown when uncertainties are larger than the points. The uncertainty shown for the monoenergetic beam data is purely statistical, while that shown for the deconvoluted data also includes statistical and systematic flux uncertainties associated with energy binning near threshold. (a) The full experimental range. The resonance at 2431 keV was too narrow for accurate deconvolution. Several points with high uncertainty, resulting from low-statistics runs, are apparent at ~ 2950 keV; these data, taken at the same energy, were combined for the purpose of deconvolution. (b) An expanded view of the boxed region near threshold better shows the differences between the two methods. The dotted (dashed) vertical line denotes the three-body (two-body) threshold. The sample photon beam profile shown (blue) is peaked at 1625 keV with an energy spread which was typical of this experiment.

211 known excited states in ${}^9\text{Be}$ [35]. These are broad states [36] which decay more strongly
 212 through the 2^+ excited state in ${}^8\text{Be}$.

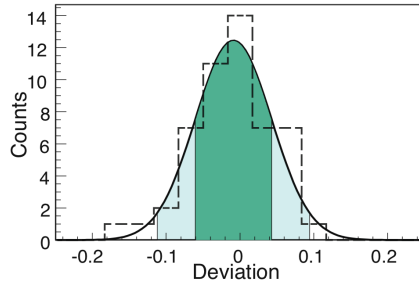


FIG. 6. (Color Online) Histogram of the relative deviation between Y and Y^* . The Gaussian fit to the error is centered just below zero. The $\pm 1\sigma$ interval is darkly shaded (teal) and the $\pm 2\sigma$ interval is shaded lightly (blue).

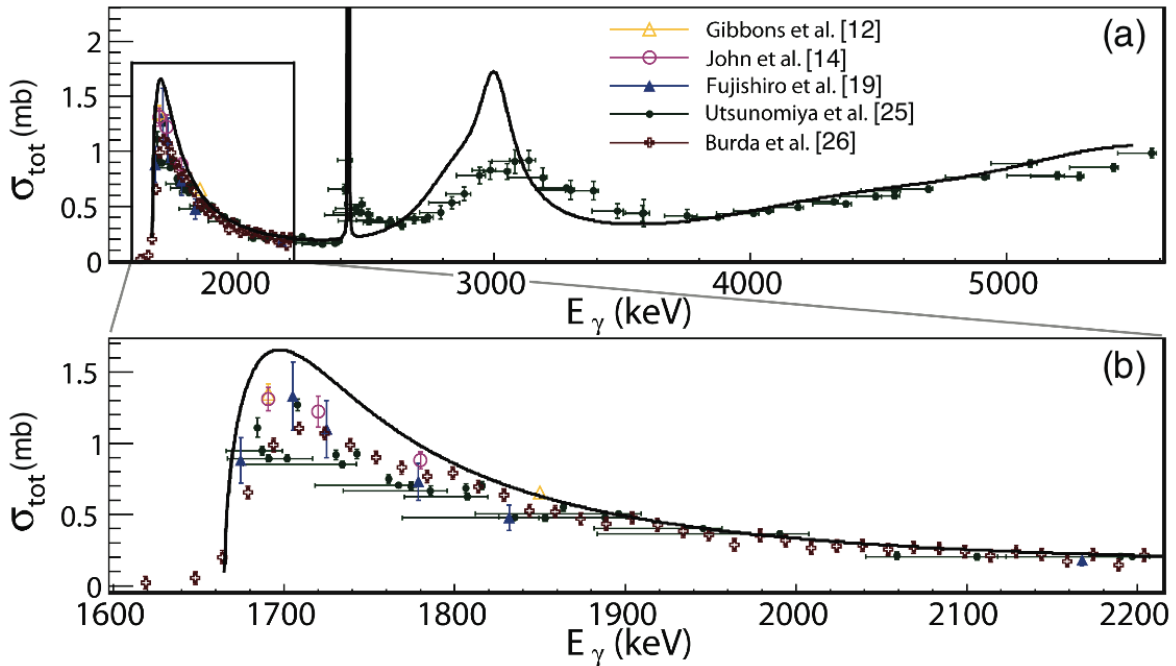


FIG. 7. (Color Online) (a) Data for the total ${}^9\text{Be}(\gamma, n){}^8\text{Be}$ cross section collected using several different γ -ray sources, including virtual photons from inelastic electron scattering [26] and real photons from both inverse Compton scattering [25] and natural radioisotopes [12, 14, 19]. (b) An expanded view of the boxed region better shows the different evaluations near the threshold.

213 **III. THRESHOLD BEHAVIOR AND ENERGY DEPENDENCE**

214 Previous measurements of the *direct* ${}^9\text{Be} + \gamma \rightarrow \alpha + \alpha + n$ three-body reaction in the energy
 215 range $1570 \text{ keV} < E_\gamma < 1670 \text{ keV}$ have yielded only an upper limit to the total cross section of
 216 93 nb [37], and the present experiment was not sufficiently sensitive to improve this. Above
 217 the two-body threshold at 1665 keV , the total ${}^9\text{Be}(\gamma, n)$ cross section rises rapidly to exceed
 218 1 mb . This feature is most logically attributed to the newly-opened decay channel, and
 219 thus excitation of the broad $1/2^+$ state located immediately above the two-body threshold
 220 is most frequently followed by decay to ${}^8\text{Be}_{gs} + n$.

221 **A. Behavior near threshold**

222 Any resonance close to threshold experiences a distortion of its normal Lorentzian cross-
 223 section shape. When a level of spin J is isolated from other levels of the same spin and
 224 parity, a one-level R-matrix approximation may be used to describe the contribution of this
 225 level to the (γ, n) cross section. For (γ, n) reactions, this takes the form of the BWE for
 226 an isolated resonance [38]:

$$\sigma_{\gamma, n}(E_\gamma) = \frac{\pi}{k_\gamma^2} \frac{2J+1}{2(2I+1)} \frac{\Gamma_\gamma \Gamma_n}{(E_\gamma - E_R)^2 + \frac{1}{4}\Gamma^2}, \quad (8)$$

227 with I the spin of the target nucleus and k_γ^2 given by

$$k_\gamma^2 = \left(\frac{E_\gamma}{\hbar c} \right)^2. \quad (9)$$

228 The neutron partial width Γ_n is generally written as [39]

$$\Gamma_n = 2\gamma^2 P_\ell, \quad (10)$$

229 where γ^2 is the reduced width and P_ℓ is the penetration factor. The reduced width incor-
 230 porates the unknown parts of the nuclear interior while P_ℓ is completely determined by the
 231 conditions outside the nucleus and may be written as

$$P_\ell = R \left(\frac{k}{F_\ell^2 + G_\ell^2} \right), \quad (11)$$

232 where R is the channel radius, k is the wave number, and ℓ is the neutron orbital angular
 233 momentum [38]. The channel radius R is defined as [38]

$$R = r_0(A_t^{1/3} + A_p^{1/3}), \quad (12)$$

234 with A_t and A_p the mass numbers of the target and projectile, respectively, and $r_0 = 1.44$ fm.
 235 For neutrons, the Coulomb wave functions, F_ℓ and G_ℓ , are related to spherical Bessel (j_ℓ)
 236 and Neumann (n_ℓ) functions by $F_\ell = (kr)j_\ell(kr)$ and $G_\ell = (kr)n_\ell(kr)$. In the cases of
 237 (γ, n) and (n, γ) reactions, the penetration factors can be written analytically, and for $0 \leq$
 238 $\ell \leq 3$, P_ℓ is [39]

$$P_0 = kR = \sqrt{\xi E_n}, \quad (13a)$$

$$P_1 = \frac{(\xi E_n)^{3/2}}{1 + \xi E_n}, \quad (13b)$$

$$P_2 = \frac{(\xi E_n)^{5/2}}{9 + 3\xi E_n + (\xi E_n)^2}, \quad (13c)$$

$$P_3 = \frac{(\xi E_n)^{7/2}}{225 + 45\xi E_n + 6(\xi E_n)^2 + (\xi E_n)^3}. \quad (13d)$$

239 In these expressions R is again the channel radius defined in Eq. 12; the neutron energy is
 240 related to the photon energy by $E_n = E_\gamma - S_n$; and we define $\xi \equiv 2\mu R^2 \hbar^{-2}$, where μ is the
 241 reduced mass of ${}^8\text{Be} + n$.

242 One must include P_ℓ energy-dependence for the $1/2^+$ threshold resonance to obtain a
 243 good fit to the ${}^9\text{Be}(\gamma, n){}^8\text{Be}$ cross-section data. However, previous works have not included
 244 energy dependence in the tails of the broad, higher-lying states in ${}^9\text{Be}$. The result of this
 245 incomplete treatment has been to inflate the previously-deduced off-resonance contributions
 246 to the $\alpha(\alpha n, \gamma){}^9\text{Be}$ rate by as much as a factor of five. The states in ${}^9\text{Be}$ excited by an
 247 $L = 1$ photon are coupled to the ground state of ${}^8\text{Be}$ through emission of a neutron with
 248 a specific orbital angular momentum ℓ determined by the spin and parity of the excited
 249 state. For the excited states considered in this paper, those with $J^\pi = 1/2^+, 1/2^-, 3/2^+,$
 250 $3/2^-, 5/2^+,$ and $5/2^-$, decay to the ground state of ${}^8\text{Be}$ through emission of a neutron with
 251 $\ell = 0, 1, 2, 1, 2,$ and 3 , respectively. The value of ℓ determines the form of P_ℓ (Eqs. 13a -
 252 13d), which in turn determines the energy dependence of the neutron partial width (defined
 253 in Eq. 10) for the excited state in ${}^9\text{Be}$, and ultimately the behavior of its cross section
 254 near the threshold. Figure 8 displays the relative contributions of the $1/2^+, 1/2^-$, and $5/2^+$
 255 resonances to the total cross section. The latter two are shown with and without the proper
 256 P_ℓ energy dependence.

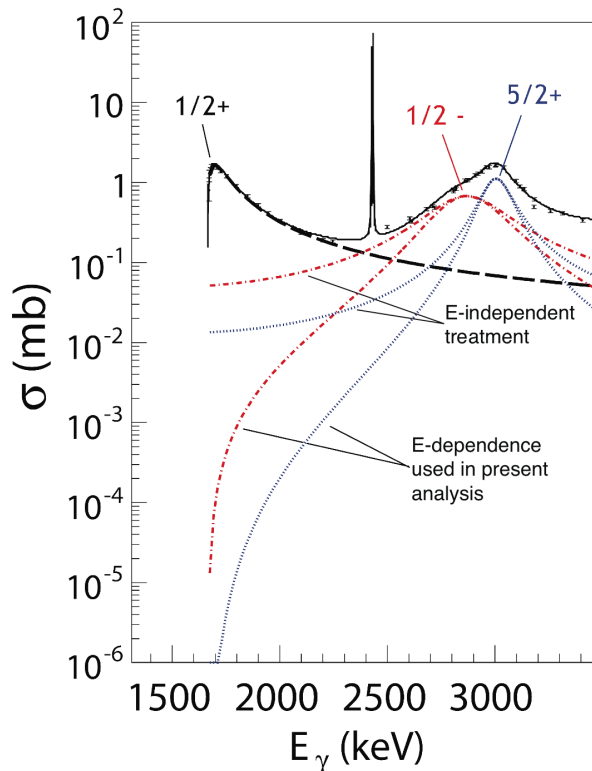


FIG. 8. (Color Online) Example of the differences between energy-independent and energy-dependent calculations of the ${}^9\text{Be}(\gamma, n){}^8\text{Be}$ cross sections at threshold. The dashed (black), dot-dashed (red) and dotted (blue) lines show the $1/2^+$, $1/2^-$, and $5/2^+$ states, respectively. Energy-dependent cross-section contributions from the $1/2^-$ and $5/2^+$ states are identified and contrasted with energy-independent determinations of these states; at threshold, the latter are orders of magnitude too large.

257 The energy-dependent γ -ray partial widths may be cast in terms of reduced transition
 258 probabilities [39]. For E1 and M1 transitions one finds

$$\Gamma_\gamma(E1) = \frac{16\pi}{9}\alpha(\hbar c)^{-2}E_\gamma^3B(E1) \downarrow, \quad (14)$$

259 and

$$\Gamma_\gamma(M1) = \frac{16\pi}{9}\alpha(2M_p c^2)^{-2}E_\gamma^3B(M1) \downarrow, \quad (15)$$

260 where α is the fine structure constant. Note that the strength of a transition from the ground
 261 state to an excited state ($B\uparrow$) is related to the strength of transition from that excited state
 262 to the ground state ($B\downarrow$) by

$$B\uparrow = \frac{2J_x + 1}{2J_0 + 1} B\downarrow. \quad (16)$$

TABLE II. Resonance parameters and neutron branching ratios from the present work. The latter were determined from the neutron detector efficiency analysis discussed in Sect. II B

J^π	χ_λ	E_R (MeV)	B(χ_λ)		Γ_n (keV)	β_j (%)
			E1 \rightarrow ($e^2\text{fm}^2$)	M1 \rightarrow (μ_N^2)		
1/2 ⁺	E1	1.731 \pm 0.002	0.136 \pm 0.002	0.738 \pm 0.002	213 \pm 6	100
5/2 ⁻	M1	2.431 \pm 0.004	0.587 \pm 0.027	0.098 \pm 0.004	0.77 ^{a,b}	6 ^c
1/2 ⁻	M1	2.880 \pm 0.016	6.5 \pm 0.7	1.8 \pm 0.2	393 \pm 18	100
5/2 ⁺	E1	3.008 \pm 0.004	0.016 \pm 0.002	0.45 \pm 0.07	163 \pm 15	70
3/2 ⁺	E1	4.704 ^b	0.068 \pm 0.007	7.8 \pm 0.4	1541 \pm 115	38
3/2 ⁻	M1	5.59 ^b	7.8 \pm 2.1	15.7 \pm 4.2	941 \pm 164	38

^a This value could not be obtained using the present data.

^b This value was fixed in accordance with Ref. [35].

^c This was fixed in accordance with Ref. [34].

263 Transitions from the ground state of ${}^9\text{Be}$, $J_0 = 3/2^-$, to an excited state, $J_x = 1/2$, $3/2$, or
264 $5/2$, yield ratios of 0.5, 1, and 1.5, respectively, in Eq. 16. Since $B \downarrow$ are the strengths of
265 transitions used in the calculation of the $\alpha(\alpha n, \gamma){}^9\text{Be}$ rate, they will be used exclusively in
266 the following discussion. For each resonance, the reduced width γ^2 , the transition strength
267 B(E1) \downarrow or B(M1) \downarrow , and the resonance energy E_R are determined by fitting the data. Table II
268 displays the parameters determined for each resonance. The sub-eV width of the narrow 5/2⁻
269 state precluded experimental determination of the associated Γ_n , and therefore the width
270 reported in Ref. [35] was adopted for the present rate calculation. Known contributions
271 from B(E2) \downarrow for the negative parity states were negligible compared to B(M1) \downarrow [35].

272 B. Narrow resonance treatment

273 In the case of narrow resonances, Γ_γ may be deduced by integrating the cross section.
274 For this to be valid: (a) the resonance must be sufficiently isolated from other resonances,
275 (b) the neutron and γ -ray partial widths must be small enough to be considered energy-
276 independent, and (c) the neutron partial width must be much larger than the γ -ray partial
277 width such that $\Gamma_n \approx \Gamma$. With these three conditions satisfied, Eq. 8 may be integrated for

TABLE III. Resonance parameters and reduced transition probabilities of the $1/2^+$ state of ${}^9\text{Be}$ from virtual and real photon experiments. Refs. [20, 24, 40] include reanalyses of data originally analyzed by Refs. [19, 21, 25], respectively.

Reaction	Ref.	E_R (MeV)	Γ_n (keV)	Γ_γ (eV)	$B(E1)\downarrow$ ($e^2\text{fm}^2$)
(e, e')	Clerc <i>et al.</i> [16]	1.78	150 ± 50	0.3	0.050 ± 0.020
(e, e')	Kuechler <i>et al.</i> [21]	1.684	217 ± 10	0.27	0.054
(e, e')	Glick <i>et al.</i> [41]	1.68	200 ± 20	0.34	0.068
(e, e')	Barker <i>et al.</i> [24]	1.732	270	0.75	0.137
(e, e')	Burda <i>et al.</i> [26]	1.748	274 ± 8	0.302 ± 0.045	0.054
(γ, n)	Barker <i>et al.</i> [20]	1.733	227 ± 50	0.577	0.106 ± 0.018
(γ, n)	Angulo <i>et al.</i> [42]	1.731	227 ± 15	0.51 ± 0.10	0.094 ± 0.020
(γ, n)	Utsunomiya <i>et al.</i> [25]	1.748	283 ± 42	0.598	0.107 ± 0.007
(γ, n)	Sumiyoshi <i>et al.</i> [40]	1.735	225 ± 12	0.568	0.104 ± 0.002
(γ, n)	Present	1.731 ± 0.002	213 ± 6	0.738 ± 0.002	0.136 ± 0.002

278 the $5/2^-$ resonance, yielding

$$\int \sigma_{\gamma,n}(E_\gamma) dE_\gamma = \frac{3}{2} \left(\frac{\hbar c \pi}{E_R} \right)^2 \Gamma_\gamma. \quad (17)$$

279 The value obtained from this analysis is shown in Table II.

280 C. The $1/2^+$ threshold resonance

281 As will be shown in Sect. IV, the $1/2^+$ threshold resonance is *the* largest contributor to
 282 the $\alpha(\alpha n, \gamma){}^9\text{Be}$ reaction rate. Table III contains resonance parameters for this state from
 283 several works. Notice that all but one of the evaluated virtual photon (e, e') data produced
 284 reduced transition strengths and γ -ray partial widths that are about half of the value of their
 285 real photon (γ, n) counterparts. The anomalous parameters within the (e, e') subset of the
 286 data [24] result from a reanalysis of the cross-section data of Ref. [21]. Indeed, an inspection
 287 of the cross-section data shown in (b) of Fig. 7 from all the works mentioned in Table III
 288 reveals that the reported cross sections are remarkably similar: the maximum difference
 289

290 between cross sections is less than a factor of two; cross sections obtained separately from
 291 real and virtual photon experiments only vary by 20% to 40%. It thus appears that different
 292 methods of data interpretation, rather than cross-section determinations, give rise to the
 293 difference in reported resonance parameters. The main difference between the analyses of
 294 Refs. [21, 26] and the present analysis involves the use by the former of Siegert's theorem
 295 for extracting the $B(E1)\downarrow$.

296 IV. $\alpha(\alpha n, \gamma)^9\text{Be}$ RATE CALCULATION

297 A. Reverse reaction cross section

298 The $^9\text{Be}(\gamma, n)^8\text{Be}$ cross section is transformed into the $^8\text{Be}(n, \gamma)^9\text{Be}$ cross-section using
 299 the reciprocity theorem. Defining σ_1 to be the cross section for $^8\text{Be} + n \rightarrow ^9\text{Be} + \gamma$, and σ_2
 300 to be the cross section for $^9\text{Be} + \gamma \rightarrow ^8\text{Be} + n$, the reciprocity theorem gives

$$\sigma_1 = \frac{2(2j_{^9\text{Be}} + 1)}{(2j_{^8\text{Be}} + 1)(2j_n + 1)} \frac{k_\gamma^2}{k_n^2} \sigma_2, \quad (18)$$

301 where $k_n^2 = 2\mu E_n \hbar^{-2}$; k_γ^2 is defined in Eq. 9; and the ground state spins for ^9Be , ^8Be , and a
 302 neutron are 3/2, 0, and 1/2, respectively.

303 For several years prior to 1999, the $\alpha(\alpha n, \gamma)^9\text{Be}$ rate used in reaction network codes was
 304 adopted from Ref. [43], which considered resonant-only decays of $^9\text{Be} + \gamma \rightarrow ^8\text{Be} + n$. In other
 305 words, when considering the $^8\text{Be} + n \rightarrow ^9\text{Be} + \gamma$ direction for the reaction, the width of the
 306 ground state of ^8Be was disregarded. The rate published by Ref. [42] (known as NACRE)
 307 included the off-resonant contributions to the $\alpha(\alpha n, \gamma)^9\text{Be}$ rate. Other rates [26, 40] have
 308 since followed the formalism developed by NACRE.

309 B. Rate calculation

310 The derivation of astrophysical reaction rates has been described in detail in Ref. [38].
 311 The rate per particle pair $\langle \sigma v \rangle$ is given by

$$\langle \sigma v \rangle = \left(\frac{8}{\pi \mu} \right)^{\frac{1}{2}} \left(\frac{1}{kT} \right)^{\frac{3}{2}} \int_0^\infty \sigma(E) \exp\left[\frac{-E}{kT} \right] E dE, \quad (19)$$

312 where μ is the particle pair reduced mass, k is Boltzmann's constant, and T is the tem-
 313 perature. Equation 19 is the appropriate form for a two-body reaction. However, here the

314 rate has to be computed for two sequential reactions. The form for calculating the rate
 315 of formation of ${}^9\text{Be}$ involves constructing a double integral, taking into account the rate of
 316 formation of ${}^8\text{Be}$ from the $\alpha + \alpha$ scattering cross sections. The formalism adopted in the
 317 present work was developed in Ref. [44] for calculating the on- and off-resonant formation
 318 of ${}^{12}\text{C}$ via the triple- α reaction, and was first modified in Ref. [42] to calculate the rate of
 319 formation of ${}^9\text{Be}$ for the NACRE compilation.

320 Two α -particles interact with center-of-mass (CM) energy E to form ${}^8\text{Be}$. Subsequently,
 321 the ${}^8\text{Be}$ nucleus interacts with a neutron with new CM energy E' relative to E (see Fig. 2).
 322 The rate equation has the form

$$\begin{aligned}
 N_A^2 \langle \sigma v \rangle^{\alpha\alpha n} &= N_A \left(\frac{8\pi\hbar}{\mu_{\alpha\alpha}^2} \right) \left(\frac{\mu_{\alpha\alpha}}{2\pi kT} \right)^{3/2} \times \\
 \int_0^\infty \frac{\sigma_{\alpha\alpha}(E)}{\Gamma_\alpha({}^8\text{Be}, E)} \exp(-E/kT) N_A \langle \sigma v \rangle^{n^8\text{Be}} E dE, & \quad (20)
 \end{aligned}$$

323 with

$$\begin{aligned}
 N_A \langle \sigma v \rangle^{n^8\text{Be}} &= N_A \left(\frac{8\pi\hbar}{\mu_{n^8\text{Be}}^2} \right) \left(\frac{\mu_{n^8\text{Be}}}{2\pi kT} \right)^{3/2} \\
 \times \int_0^\infty \sigma_{n^8\text{Be}}(E'; E) \exp(-E'/kT) E' dE'. & \quad (21)
 \end{aligned}$$

324 Equation 20 is evaluated numerically using the parameters from Table II and the $\alpha +$
 325 α scattering cross-sections from Ref. [45] over the temperature range $0.001 \text{ GK} \leq T \leq 10$
 326 GK. Table IV lists low, recommended, and high values for the presently determined rates
 327 versus temperature. The low and high rates are computed by considering the systematic
 328 uncertainty in the deconvoluted ${}^9\text{Be}(\gamma, n){}^8\text{Be}$ cross section and the uncertainty in the fitting
 329 parameters (see Table II). At all temperatures, the $\alpha(\alpha n, \gamma){}^9\text{Be}$ rate originates primarily
 330 from the $1/2^+$ state in ${}^9\text{Be}$ (see Fig. 9). Thus, the rate uncertainty is dominated by the cross-
 331 section uncertainty for that state. Uncertainty in the rate increases at higher temperatures,
 332 where higher states in ${}^9\text{Be}$ begin to contribute noticeably to the $\alpha(\alpha n, \gamma){}^9\text{Be}$ reaction rate.

TABLE IV: Low, recommended, and high rates for the $\alpha(\alpha n, \gamma)^9\text{Be}$ reaction versus T_9 ($\equiv 1 \text{ GK}$) computed from the present parameters.

T_9	$N_A\langle\alpha\alpha n\rangle$			T_9	$N_A\langle\alpha\alpha n\rangle$		
	Low	Recommended	High		Low	Recommended	High
0.001	1.15E-59	1.20E-59	1.26E-59	0.14	4.39E-08	4.62E-08	4.84E-08
0.002	9.64E-48	1.01E-47	1.06E-47	0.15	6.49E-08	6.82E-08	7.14E-08
0.003	6.01E-42	6.32E-42	6.62E-42	0.16	9.05E-08	9.51E-08	9.96E-08
0.004	2.76E-38	2.90E-38	3.04E-38	0.18	1.54E-07	1.62E-07	1.70E-07
0.005	1.12E-35	1.18E-35	1.24E-35	0.2	2.32E-07	2.43E-07	2.55E-07
0.006	1.11E-33	1.17E-33	1.23E-33	0.25	4.49E-07	4.72E-07	4.95E-07
0.007	4.40E-32	4.62E-32	4.84E-32	0.3	6.51E-07	6.84E-07	7.17E-07
0.008	9.21E-31	9.67E-31	1.01E-30	0.35	8.07E-07	8.48E-07	8.89E-07
0.009	1.21E-29	1.27E-29	1.33E-29	0.4	9.10E-07	9.57E-07	1.00E-06
0.01	1.12E-28	1.18E-28	1.24E-28	0.45	9.70E-07	1.02E-06	1.07E-06
0.011	7.90E-28	8.31E-28	8.71E-28	0.5	9.94E-07	1.04E-06	1.10E-06
0.012	4.47E-27	4.70E-27	4.93E-27	0.6	9.76E-07	1.03E-06	1.07E-06
0.013	2.12E-26	2.22E-26	2.33E-26	0.7	9.10E-07	9.56E-07	1.00E-06
0.014	8.64E-26	9.08E-26	9.52E-26	0.8	8.29E-07	8.71E-07	9.13E-07
0.015	3.12E-25	3.28E-25	3.43E-25	0.9	7.45E-07	7.83E-07	8.21E-07
0.016	1.01E-24	1.06E-24	1.12E-24	1	6.66E-07	7.00E-07	7.34E-07
0.018	8.24E-24	8.65E-24	9.07E-24	1.25	5.02E-07	5.28E-07	5.53E-07
0.02	5.09E-23	5.35E-23	5.61E-23	1.5	3.83E-07	4.02E-07	4.22E-07
0.025	2.51E-21	2.64E-21	2.77E-21	1.75	2.98E-07	3.13E-07	3.28E-07
0.03	4.31E-19	4.53E-19	4.75E-19	2	2.37E-07	2.49E-07	2.61E-07
0.04	1.81E-15	1.90E-15	2.00E-15	2.5	1.58E-07	1.66E-07	1.74E-07
0.05	2.63E-13	2.76E-13	2.90E-13	3	1.12E-07	1.18E-07	1.24E-07
0.06	6.88E-12	7.23E-12	7.58E-12	3.5	8.43E-08	8.88E-08	9.33E-08
0.07	6.81E-11	7.15E-11	7.50E-11	4	6.59E-08	6.95E-08	7.32E-08
0.08	3.68E-10	3.87E-10	4.06E-10	5	4.41E-08	4.67E-08	4.94E-08

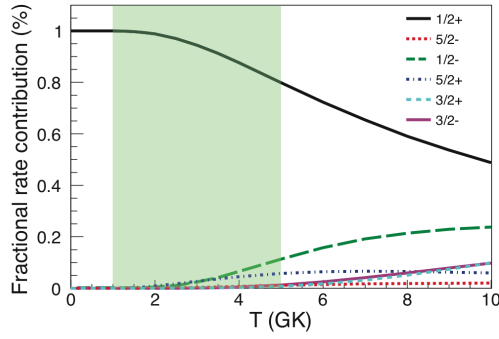


FIG. 9. (Color Online) Relative contributions of each resonance to the total rate as a function of temperature. The temperature range relevant for the r-process, $1 \text{ GK} < T < 5 \text{ GK}$, is shaded (green).

TABLE IV: (Continued)

T_9	$N_A \langle \alpha \alpha n \rangle$			T_9	$N_A \langle \alpha \alpha n \rangle$		
	Low	Recommended	High		Low	Recommended	High
0.09	1.34E-09	1.40E-09	1.47E-09	6	3.22E-08	3.43E-08	3.65E-08
0.1	3.67E-09	3.86E-09	4.05E-09	7	2.49E-08	2.68E-08	2.86E-08
0.11	8.27E-09	8.69E-09	9.11E-09	8	2.02E-08	2.18E-08	2.35E-08
0.12	1.60E-08	1.68E-08	1.77E-08	9	1.69E-08	1.84E-08	1.99E-08
0.13	2.77E-08	2.92E-08	3.06E-08	10	1.46E-08	1.59E-08	1.74E-08

333 Figure 10 displays the comparison of four existing rates both by their absolute magni-
334 tudes and by normalization to the NACRE rate [42]. The present rate is 40% larger than
335 the NACRE result for the energy range $1 \text{ GK} < T < 5 \text{ GK}$, most important for r-process
336 nucleosynthesis. The largest difference between the various rates exists in the off-resonant
337 region: there the present rate is smaller than the NACRE rate by a factor of 4 because the
338 energy dependence of all resonant cross-section contributions near the two-body threshold
339 has been included.

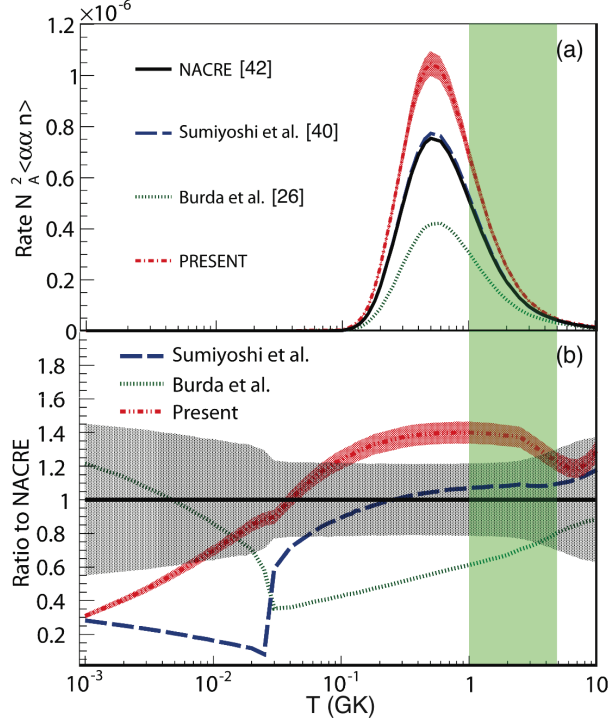


FIG. 10. (Color Online)(a) The reaction rate as a function of temperature. The present rate is 40% larger than the rates of Refs. [40] and [42] at the peak near $T = 0.5$ GK. The temperature range relevant for the r-process, $1 \text{ GK} < T < 5 \text{ GK}$, is shaded (green). (b) The ratio of the rates to the NACRE rate. Bands shown indicate $\pm 1\sigma$ uncertainties for NACRE and the present rate.

340 C. Rate comparisons

341 In principle, the precision of the measured ${}^9\text{Be}(\gamma, n){}^8\text{Be}$ reaction cross section should
 342 extend to the deduced astrophysical $\alpha(\alpha n, \gamma){}^9\text{Be}$ rate. The quantities used for calculating
 343 the $\alpha + \alpha \rightarrow {}^8\text{Be}$ rate derive from well known $\alpha + \alpha$ scattering data [45], while accurate
 344 penetration factors are obtained from computed Coulomb wave functions. Recalling Fig.
 345 10, the present rate, when compared to the NACRE rate, is a factor of 3 lower at the lowest
 346 calculated temperatures, while it is 20% to 40% larger at astrophysical temperatures of
 347 interest for the r-process ($1 \text{ GK} < T < 5 \text{ GK}$). The change of the low-temperature rate is
 348 a direct result of including a realistic energy dependence for all neutron partial widths, a
 349 procedure which was not employed in Ref. [42]. The correct analytic form for s -, p -, and d -
 350 wave neutron penetration factors lowers all resonant contributions near threshold as shown
 351 in Fig. 8. At low temperatures, the energy-independent treatment leads to an artificially

352 inflated rate along with the non-physical dominant contributions to this rate by the p -wave
353 $1/2^-$ and d -wave $5/2^+$ states.

354 Recently, Garrido *et al.* [46] have used three-body theoretical techniques to determine
355 the direct $\alpha + \alpha + n \rightarrow {}^9\text{Be}$ contribution to both the total cross section and reaction rate at
356 energies below the two-body threshold. However, their calculated direct, three-body cross
357 section exceeds the 93 nb experimental upper limit [37] at energies between the three- and
358 two-body thresholds. The results presented in the present paper consider only sequential
359 reactions and do not address the possibility of contributions by three-body processes at the
360 lowest temperatures.

361 The present $\alpha(\alpha n, \gamma){}^9\text{Be}$ rate for $1 \text{ GK} \leq T \leq 5 \text{ GK}$ is consistently 20% to 40% larger
362 than the rates of Refs. [40, 42]. Agreement with the NACRE rate marginally improves as
363 the temperature approaches 10 GK. Figure 9 shows that, for the present evaluation, the
364 $1/2^+$ state is indeed the primary contributor to the rate at temperatures below 10 GK. Con-
365 tributions from other states start to become noticeable for $T \geq 5 \text{ GK}$. This implies that the
366 choice of branching ratios is not important for an accurate $\alpha(\alpha n, \gamma){}^9\text{Be}$ rate determination.

367 V. CONCLUSIONS

368 The improved accuracy of the measurement of the ${}^9\text{Be}(\gamma, n){}^8\text{Be}$ reaction cross section
369 reported in this work was made possible: a) by use of a highly-efficient neutron detector
370 with two concentric, circular arrays of ${}^3\text{He}$ tubes which provided information about the
371 energy distribution of the detected neutrons; b) by calibration of the neutron detector's
372 efficiency using interspersed measurement of the well-known ${}^2\text{H}(\gamma, n)$ cross section; and c)
373 by measuring at each energy both the flux and energy distribution of the incident γ -ray
374 beam used. Knowledge of the incident beam's energy distribution allowed deconvolution
375 and determination of the cross section near the neutron threshold at 1665 keV. These new
376 measurements have been used to calculate the astrophysical $\alpha(\alpha n, \gamma){}^9\text{Be}$ reaction rate.

377 Taking into account energy dependence of all neutron and γ -ray partial widths near
378 threshold gives rise to smaller rates than previously calculated for $T \leq 0.025 \text{ GK}$. For $T \geq 2$
379 GK, contributions to the rate from higher-lying resonances become noticeable. Our cross
380 sections and the resulting astrophysical reaction rates in the temperature range $1 \text{ GK} \leq T \leq 5$
381 GK are 20% to 40% larger than previously reported. The present rate is computed using a

382 cross section known to $\pm 10\%$ at the 95% confidence level. This new rate should be employed
383 in reaction network codes, especially those used to investigate r-process nucleosynthesis sites.

384 ACKNOWLEDGMENTS

385 This work was supported in part by USDOE Office of Nuclear Physics Grants DE-
386 FG02-97ER41041 and DE-FG02-97ER41033. We wish to acknowledge the staff of the UNC
387 Chapel Hill and Duke instrument shops; experimental collaborators G. Rusev, S. Stave,
388 M.W. Ahmed, and Y. Wu; and the HI γ S accelerator staff for their help in completing these
389 measurements.

-
- 390 [1] S. E. Woosley, J. R. Wilson, G. J. Mathews, R. D. Hoffman, and B. S. Meyer, *Astrophys. J.*,
391 **433**, 229 (1994).
- 392 [2] C. Freiburghaus, S. Rosswog, and F.-K. Thielemann, *Astrophys. J.*, **525**, 121 (1999).
- 393 [3] Y.-Z. Qian and G. Wasserburg, *Phys. Rep.*, **442**, 237 (2007).
- 394 [4] T. Sasaqui, K., T. Kajino, G. Mathews, K. Otsuki, and T. Nakamura, *Astrophys. J.*, **634**,
395 1173 (2005).
- 396 [5] S. Woosley and T. Janka, *Nat. Phys.*, 147 (2005).
- 397 [6] H.-T. Janka, K. Langanke, A. Marek, G. Martínez-Pinedo, and B. Müller, *Phys. Rep.*, **442**,
398 38 (2007).
- 399 [7] S. E. Woosley and R. D. Hoffman, *Astrophys. J.*, **395**, 202 (1992).
- 400 [8] M. Terasawa, K. Sumiyoshi, T. Kajino, G. Mathews, and I. Thanihata, *Astrophys. J.*, **562**,
401 470 (2001).
- 402 [9] T. Sasaqui, K. Otsuki, T. Kajino, and G. Mathews, *Astrophys. J.*, **645**, 1345 (2006).
- 403 [10] R. Surman and G. McLaughlin, “Private communication,” (2010).
- 404 [11] A. Mengoni and T. Otsuka, *AIP Conference Proceedings*, **529**, 119 (2000).
- 405 [12] J. H. Gibbons, R. L. Macklin, J. B. Marion, and H. W. Schmitt, *Phys. Rev.*, **114**, 1319 (1959).
- 406 [13] M. J. Jakobson, *Phys. Rev.*, **123**, 229 (1961).
- 407 [14] W. John and J. M. Prosser, *Phys. Rev.*, **127**, 231 (1962).
- 408 [15] B. L. Berman, R. L. V. Hemert, and C. D. Bowman, *Phys. Rev.*, **163**, 958 (1967).

- 409 [16] H.-G. Clerc, K. Wetzel, and E. Spamer, Nucl. Phys. A, **120**, 441 (1968).
- 410 [17] A. Salyers, Phys. Rev. C, **2**, 1653 (1970).
- 411 [18] R. J. Hughes, R. H. Sambell, E. G. Muirhead, and B. M. Spicer, Nucl. Phys. A, **238**, 189
412 (1975).
- 413 [19] M. Fujishiro, T. Tabata, K. Okamoto, and T. Tsujimoto, Can. J. Phys., **60**, 1672 (1982).
- 414 [20] F. Barker, Can. J. Phys., **61**, 1371 (1983).
- 415 [21] G. Kuechler, A. Richter, and W. von Witsch, Z. Phys. A, **326**, 447 (1987).
- 416 [22] A. M. Goryachev, G. N. Zalesny, and I. V. Pozdnev, Bull. Russ. Acad. Sci. Phys., **56** (1992).
- 417 [23] V. Efros, H. Oberhummer, A. Pushkin, and I. Thompson, Eur. Phys. J. A, 447 (1998).
- 418 [24] F. Barker, Aus. J. Phys., **53**, 247 (2000).
- 419 [25] H. Utsunomiya, Y. Yonezawa, H. Akimune, T. Yamagata, M. Ohta, M. Fujishiro, H. Toyokawa,
420 and H. Ohgaki, Phys. Rev. C, **63**, 018801 (2000).
- 421 [26] O. Burda, P. von Neumann-Cosel, A. Richter, C. Forssén, and B. A. Brown, Phys. Rev. C,
422 **82**, 015808 (2010).
- 423 [27] C. W. Arnold, T. B. Clegg, H. J. Karwowski, G. C. Rich, J. R. Tompkins, and C. R. Howell,
424 Nucl. Instrum. Meth. A, **647**, 55 (2011).
- 425 [28] H. R. Weller, M. W. Ahmed, H. Gao, W. Tornow, Y. K. Wu, M. Gai, and R. Miskimen,
426 Prog. Part. Nucl. Phys., **62**, 257 (2009).
- 427 [29] R. Schiavilla, Phys. Rev. C, **72**, 034001 (2005).
- 428 [30] C. Sun, Ph.D. thesis, Duke University (2009).
- 429 [31] T. Black, B. Hendrix, E. Crosson, K. Fletcher, H. Karwowski, and E. Ludwig, Nucl. Instrum.
430 Meth. A, **333**, 239 (1993).
- 431 [32] C. W. Arnold, Ph.D. thesis, UNC Chapel Hill (2011).
- 432 [33] C. W. Arnold, T. B. Clegg, C. R. Howell, H. J. Karwowski, G. C. Rich, and J. R. Tompkins,
433 TUNL Progress Report, **XLIX** (2010).
- 434 [34] P. R. Christensen and C. L. Cocke, Nucl. Phys., **89**, 656 (1966).
- 435 [35] D. Tilley, J. Kelley, J. Godwin, D. Millener, J. Purcell, C. Sheu, and H. Weller, Nucl. Phys.
436 A, **745**, 155 (2004).
- 437 [36] S. Dixit *et al.*, Phys. Rev. C, **43**, 1758 (1991).
- 438 [37] D. E. Alburger, R. E. Chrien, R. J. Sutter, and J. F. Wishart, Phys. Rev. C, **70**, 064611
439 (2004).

- 440 [38] C. Iliadis, *Nuclear Physics of Stars* (Wiley-VCH, Weinheim, 2007).
- 441 [39] J. M. Blatt and V. F. Weisskopf, *Theoretical Nuclear Physics* (John Wiley & Sons, Inc., New
442 York, 1952).
- 443 [40] K. Sumiyoshi, H. Utsunomiya, S. Goko, and T. Kajino, *Nucl. Phys. A*, **709**, 467 (2002).
- 444 [41] J. P. Glickman *et al.*, *Phys. Rev. C*, **43**, 1740 (1991).
- 445 [42] C. Angulo *et al.*, *Nucl. Phys. A*, **656**, 3 (1999).
- 446 [43] G. R. Caughlan and W. A. Fowler, *At. Data Nucl. Data Tables*, **40**, 283 (1988).
- 447 [44] K. Nomoto, F. Thielemann, and S. Miyaji, *Astron. Astrophys.*, **149**, 239 (1985).
- 448 [45] S. Wüstenbecker *et al.*, *Z. Phys. A*, **326**, 205 (1992).
- 449 [46] E. Garrido, R. de Diego, D. Fedorov, and A. Jensen, *Eur. Phys. J. A*, **47**, 1 (2011).